Orthogonal tight-binding model for the thermal conductivity of Si

Ankita Katre[*] and Georg K. H. Madsen

ICAMS, Ruhr-Universität Bochum, 44801 Bochum, Germany

Predictive modeling of the thermal conductivity of nanostructures remains a large challenge. *Ab initio* studies rely on parametrized models of scattering rates of the nanostructure elements. Simplified interatomic potentials, on the other hand, often fail in the quantitative prediction of thermal conductivity. We have developed a simple and short-ranged orthogonal tight-binding model for the thermal properties of Si. We systematically introduce separate handles to tune the value and slope of the potential energy with respect to interatomic distance. Furthermore, we add an embedding potential in our model to capture the correct structural stability trend in Si. The model shows excellent transferability to the thermal properties of diamond Si along with good reproduction of the relative stabilities of different structures. We demonstrate the improvement over earlier tight-binding models and contrast the transferability of our model with simple interatomic potentials.

I. INTRODUCTION

Silicon is one of the most important industrial materials due to its favorable technological properties and abundance. Bulk Si as well as its different alloys and nanostructures are commercially used in a wide variety of applications such as thermoelectrics, nanoelectronics, solar cells, power devices, biomedical instruments, etc. [1–8]. Thermal conductivity is a crucial property for improving the performances of these devices, directly affecting the efficiency of thermoelectric materials and the lifetimes and performance of electronic devices [9].

Theoretical studies of thermal transport in nanomaterials are challenging due to the complexity of the nanostructures and the theoretical method. A conceptually simple method as molecular dynamics (MD) can be used to calculate thermal conductivity for these structures directly. However, due to the involved time and length scales, these MD simulations are generally based on classical empirical potentials. This leads to both lack of transferability and poor agreement with experiments [10–12]. On the other hand, density functional theory (DFT) based thermal conductivity calculations using the Boltzmann transport equation (BTE) show excellent agreement with experiments [13–16]. The method is however limited to bulk materials and the role of alloying and nanostructuring has to be included through model scattering rates [14,17–19].

The tight-binding (TB) scheme offers a compromise in this respect, as it is more precise than the empirical potentials and computationally less demanding than DFT. The TB scheme provides an elegant way to include quantum bonding effects in a simplified model of interatomic bonding. Although based on a similar philosophy as the linear combination of atomic orbitals in DFT, the TB scheme drastically reduces the computational cost by using a minimal basis with parametrized integrals and a total energy functional. Furthermore, short-ranged orthogonal tight-binding (OTB) models make it less complex to implement methods where the computational time scales linearly with a number of atoms [20].

In the present paper we develop a simple and short-ranged OTB model and compare it to available OTB models for calculating the thermal conductivity of Si. This paper is structured as follows: The DFT computational details and the approach to calculate thermal conductivity and other thermal properties are elaborated in Sec. II A. The OTB modeling scheme is introduced in Sec. II B. We review earlier OTB models in Sec. III A for their performances in calculating thermal properties of Si, before presenting an OTB model in Sec. III B. The recursive process of model parametrization and its applicability to predict correct binding energy trends for different structures of Si is elaborated in Sec. III. The thermal properties of diamond and clathrate-*I* Si with our model are also discussed in Sec. III, followed by a conclusion in Sec. IV.

II. METHODOLOGY

A. Computational details

We have performed reference *ab initio* calculations of the energetics and thermal properties for different Si structures. The DFT calculations for these structures are done with a projector augmented wave method [21] as implemented in the VASP package [22]. The plane wave energy cutoff of 350 eV is used for all the calculations. A dense Monkhorst-Pack **k**-point mesh of $16 \times 16 \times 16$ is employed for all the structures of Si except for the clathrate-*I* Si where we have used $8 \times 8 \times 8$ **k**-point mesh. The earlier TB models are compared to DFT calculations using the PW92 local density approximation (LDA) [23] as those models were fitted to LDA data sets. The PBE [24] generalized gradient approximation is used for the reference data to parametrize our model.

For the evaluation of thermal properties, the *ab initio* force calculations on $4 \times 4 \times 4$-fcc diamond Si (128 atoms) and $2 \times 2 \times 2$-fcc clathrate-*I* Si (92 atoms) supercells are performed with accordingly smaller **k**-point mesh. We have used the finite displacement method and have calculated the forces on all the atoms in supercells with symmetry reduced atomic displacement of 0.06 Å. The amplitude was tested for convergence in our earlier study [18]. The force constants are extracted from these calculations using the program PHONOPY [25]. The thermal expansion α is evaluated within

---
*ankitamkatre@gmail.com

the quasiharmonic approximation using $\pm 9\%$ cell volume range for the force calculations. In the finite displacement method, the third-order force constants Ψ are obtained in terms of net atomic forces as [26]

$$\Psi_{\alpha_1 \alpha_2 \alpha_3}(l\boldsymbol{b}, l'\boldsymbol{b}', l''\boldsymbol{b}'')$$
$$\simeq -\frac{F_{\alpha_3}(l''\boldsymbol{b}'')[\boldsymbol{u}(l\boldsymbol{b})\boldsymbol{u}(l'\boldsymbol{b}')] - F_{\alpha_3}(l''\boldsymbol{b}'')[\boldsymbol{u}(l'\boldsymbol{b}')]}{u_{\alpha_1}(l\boldsymbol{b})u_{\alpha_2}(l'\boldsymbol{b}')}, \quad (1)$$

where $\boldsymbol{u}$ represents the displacement of atoms with position vectors $\boldsymbol{b}, \boldsymbol{b}', \boldsymbol{b}''$ in unit cells identified by vectors l, l', l'' and F_{α_3} denotes the α_3 component of the force on an atom at $\boldsymbol{b}''l''$. The force calculations for third-order force constants are performed for diamond Si with same supercell size, displacement, and *ab initio* parameters as used for harmonic calculations. We have considered all the symmetry reduced pair displacements, without any cutoff, for our calculations. The PHONO3PY package [27] is used for extracting third-order force constants and calculating phonon-phonon scattering rates using the tetrahedron method and a converged $\mathbf{q}$ mesh of $40 \times 40 \times 40$.

The lattice thermal conductivity κ_l of diamond Si is calculated using the BTE in the relaxation time approximation (RTA). Within the RTA, κ_l for a cubic lattice is given as

$$\kappa_l = \frac{1}{3} \sum_j \int \frac{d\mathbf{q}}{(2\pi)^3} C_{j\mathbf{q}} v_{j\mathbf{q}}^2 \tau_{j\mathbf{q}}, \quad (2)$$

where $j\mathbf{q}$ represents the phonon mode and C, v, and τ are the phonon heat capacity, velocity, and relaxation time, respectively. τ depends on the third-order force constants through the three phonon coupling strengths $|\tilde{\Psi}(-j\mathbf{q}, j'\mathbf{q}', j''\mathbf{q}'')|^2$ [13–16,27]. $|\tilde{\Psi}(-j\mathbf{q}, j'\mathbf{q}', j''\mathbf{q}'')|^2$ are obtained from the Fourier transform of the mode projected third-order force constants. Using Fermi's golden rule the scattering rate due to the phonon-phonon coupling is obtained as

$$\frac{1}{\tau_{\text{anh}, j\mathbf{q}}} = \pi \sum_{j'j''\mathbf{q}'} |\tilde{\Psi}(-j\mathbf{q}, j'\mathbf{q}', j''\mathbf{q}'')|^2$$
$$\times [(\eta_{j'\mathbf{q}'} + \eta_{j''\mathbf{q}''} + 1)\delta(\omega_{j\mathbf{q}} - \omega_{j'\mathbf{q}'} - \omega_{j''\mathbf{q}''})$$
$$+ 2(\eta_{j'\mathbf{q}'} - \eta_{j''\mathbf{q}''})\delta(\omega_{j\mathbf{q}} + \omega_{j'\mathbf{q}'} - \omega_{j''\mathbf{q}''})]. \quad (3)$$

The phonon-isotope scattering rates, calculated as in Ref. [18], are also included for thermal conductivity evaluation of diamond Si. The method for calculating κ_l, Eqs. (2) and (3), is based on the RTA and description of anharmonic contributions only up to third order. However, in combination with DFT, it has been successful in determining the κ_l in good agreement with experiment for a number of materials including diamond Si [13–15,18,19].

To calculate the κ_l for the clathrate structure, we have used a model recently proposed by us. Within this model, the scattering term is based on the quasiharmonic approximation [28,29]

$$\tau_{\text{M}}^{-1} = p\omega^2 \frac{T}{\tilde{\theta}_D} e^{-\frac{\tilde{\theta}_D}{3T}}, \quad (4)$$

where p depends on the sound velocity, the Debye temperature obtained from the second moment of the phonon density of states (pDOS), and a mode averaged squared Grüneisen parameter evaluated at the Debye temperature $\tilde{\theta}_D$ [29]. The model has been shown to give a good reproduction of

experimental lattice thermal conductivity over a wide range of magnitudes [29]. Furthermore, the lattice thermal conductivity can be split into two material dependent quantities [28] by taking $(\omega^2 \tau_{\text{M}})$ out of the integral in Eqs. (2) and (4) so that

$$\kappa_l^{\text{M}}(T) = (\omega^2 \tau_{\text{M}})\overline{(v/\omega)^2}, \quad (5)$$

with

$$\overline{(v/\omega)^2} = \frac{1}{3} \sum_j \int \frac{d\mathbf{q}}{8\pi^3} (v_{j\mathbf{q}}/\omega_{j\mathbf{q}})^2 C_{j\mathbf{q}}. \quad (6)$$

The quantities $(\omega^2 \tau_{\text{M}})$ and $\overline{(v/\omega)^2}$ can be viewed as effective parameters which represent the average phonon lifetime and velocity, respectively.

B. Orthogonal TB scheme

For a TB model of Si, a minimal basis consisting of one s and three p orbitals is sufficient for each atom. The bonding is then described with the bond integrals $\beta_{ss\sigma}$, $\beta_{sp\sigma} = -\beta_{ps\sigma}$, $\beta_{pp\sigma}$, and $\beta_{pp\pi}$, within the Slater-Koster two-center approximation [30]. These orbital interactions represent the TB Hamiltonian matrix elements in the bond-oriented coordinate system and the intersite H elements are obtained by rotating them to the global Cartesian coordinate system,

$$H_{I\mu J\nu'} = \sum_{\mu'\nu'} M_{I\mu J\nu'}^T \beta_{I\mu' J\nu'} M_{I\mu' J\nu}, \quad (7)$$

where I, J are atomic indices, μ, ν represent valence s and p orbitals, and M represents the rotation matrix. Furthermore, the on-site H elements

$$\epsilon_{I\mu}^{(0)} = H_{I\mu I\mu} = \langle I\mu|\hat{H}|I\mu\rangle \quad (8)$$

correspond to the reference orbital energies $\epsilon_s^{(0)}$ and $\epsilon_p^{(0)}$.

The parametrized TB Hamiltonian can be used further to calculate the bond energy E_{bond} for Si as

$$E_{\text{bond}} = 2 \sum_{I\mu J\nu}^{I \neq J} H_{I\mu J\nu} \rho_{I\mu J\nu}, \quad (9)$$

where $\rho_{I\mu J\nu}$ represents the density matrix elements. The multiplicative factor of 2 is used in Eq. (9) because of the spin degeneracy in Si.

Along with the bond energy, Eq. (9), the TB binding energy E_{TB} for Si has further contributions given as

$$E_{\text{TB}} = E_{\text{bond}} + E_{\text{prom}} + E_{\text{rep}}. \quad (10)$$

Local charge neutrality is self-consistently enforced and Eq. (10) neglects the charge transfer contribution, which is a reasonable approximation for elemental TB models. In Eq. (10), E_{prom} is the promotion energy which accounts for the repopulation of the on-site levels after bond formations. It is given as

$$E_{\text{prom}} = \sum_{I\mu} \epsilon_{I\mu}^{(0)}\left(N_{e\,I\mu} - N_{e\,I\mu}^{(0)}\right), \quad (11)$$

where $N_{e\,I\mu}$ and $N_{e\,I\mu}^{(0)}$ are the number of electrons in the bonded and the free atoms, respectively. Furthermore, the repulsive contribution E_{rep} is given as the sum over all the pairwise
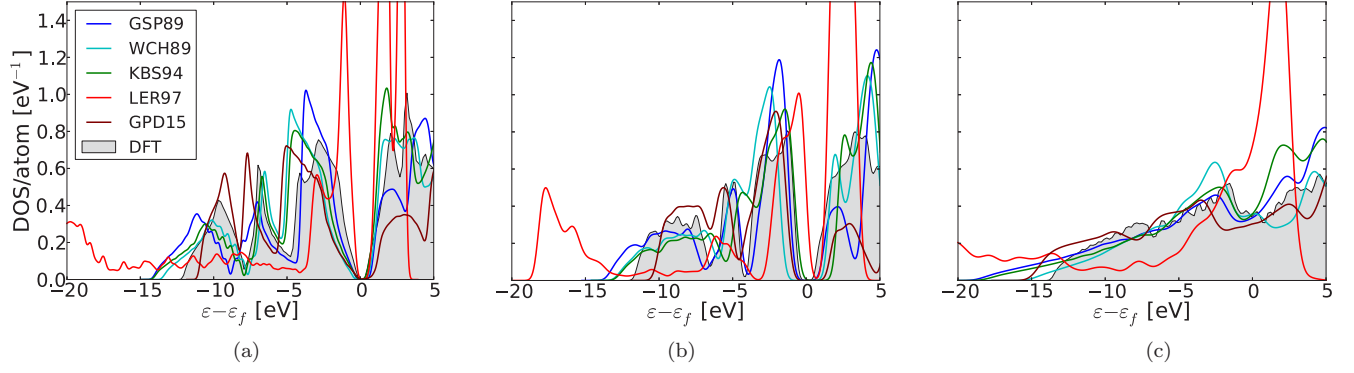
FIG. 1. DOS for Si in (a) diamond, (b) clathrate-I, and (c) β-tin structures at respective DFT optimized volumes calculated using earlier tight-binding models and compared to DFT.

repulsive energies ϕ parametrized as a function of the interatomic distance

$$E_{\rm rep} = \sum_{IJ}^{I \neq J} \phi(R_{IJ}).$$ (12)

The methodology to calculate the thermal properties of Si with the TB models is the same as that used for the DFT calculations. The only difference is in the use of TB model calculated forces in place of DFT to extract the second- and third-order force constants. For an OTB the forces can be straightforwardly calculated using the Hellmann-Feynmann theorem,

$$
\begin{aligned}
F_{\rm TB} &= F_{\rm bond} + F_{\rm rep} \\
&= 2 \sum_{I\mu J\nu}^{I \neq J} \langle I\mu | \frac{\partial \hat{H}}{\partial R_{IJ}} | J\nu \rangle + \sum_{IJ}^{I \neq J} \frac{\partial \phi(R_{IJ})}{\partial R_{IJ}}.
\end{aligned}
$$ (13)

III. RESULTS AND DISCUSSION

A. Earlier TB models

Before developing a model we test the performances of earlier OTB models, which we label GSP89 [33], WCH89 [34], KBS94 [35], LER97 [36], and GPD15 [37] after their authors and year of publication.

The early WCH89 [34] model parametrized the β's using Harrison's universal R^{-2} trend by fitting to the electronic

band structure of diamond Si at a range of volumes. The repulsive ϕ parameters were fitted to the energy-volume curve for diamond Si [34]. The model is based on only including the nearest neighbor atomic interactions for the calculations. Figure 1 shows the electronic density of states (DOS) for three low energy structures of Si, diamond, clathrate-I, and β-tin, where the WCH89 model exhibits a reasonable agreement with DFT, however with overestimated bandwidths for all three structures. The thermal properties for diamond Si with the WCH89 model are shown in Fig. 2. The pDOS and α are reproduced in good comparison to DFT, Figs. 2(a) and 2(b). However, κ_l overestimation can be seen in Fig. 2(c) which is due to the slight deviations in both the acoustic phonons, which have the contributions from the long-ranged interactions, and the phonon bandwidth, which affects the acoustic-optic phonon scattering.

The GSP89 model introduced a "rescaling" method for parametrization of β and ϕ in terms of R as [33]

$$\beta_{\mu\nu\lambda}(R) = \beta_{\mu\nu\lambda}^0 \left(\frac{R_0}{R} \right)^n \exp \left\{ n \left[-\left(\frac{R}{R_c} \right)^{n_c} + \left(\frac{R_0}{R_c} \right)^{n_c} \right] \right\},$$ (14)

where $\lambda = \sigma, \pi$ is the symmetry label, and

$$\phi(R) = \phi^0 \left(\frac{R_0}{R} \right)^m \exp \left\{ m \left[-\left(\frac{R}{R_c} \right)^{n_c} + \left(\frac{R_0}{R_c} \right)^{n_c} \right] \right\}.$$ (15)
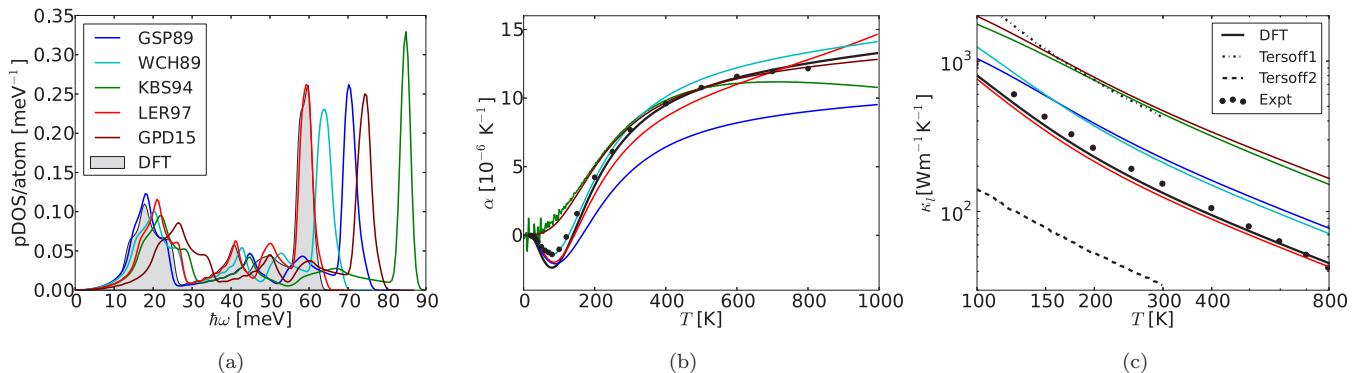

FIG. 2. (a) Phonon DOS (pDOS), (b) thermal expansion (α) (experiment from Ref. [31]), and (c) lattice thermal conductivity (κ_l) (experiment from Ref. [32]) of diamond Si with earlier OTB models compared to DFT. The κ_l with the Tersoff potentials are taken from Ref. [10].

In Eqs. (14) and (15) β^0 and ϕ^0 represent the bond integrals and pairwise repulsive potential at equilibrium interatomic distance R_0, respectively. Other fitting parameters include R_c, the bonding and repulsive slope parameters n, m, and damping parameter n_c. At equilibrium we get $\beta_{\mu\nu\lambda}(R_0) = \beta^0_{\mu\nu\lambda}$ and $\phi(R_0) = \phi^0$. For $R \neq R_0$, the exponential terms rescale the $\beta^0_{\mu\nu\lambda}$ and ϕ^0 to get the β and ϕ at particular R. The model was fitted to a small data set of diamond and fcc equilibrium volume, energies, and bulk moduli.

The GSP89 model is seen to overestimate the DOS bandwidth somewhat for all three structures, Fig. 1. The Si thermal properties calculated with the GSP89 model are seen in Fig. 2. Two main features are noticed in the pDOS, Fig. 2(a). First of all the acoustic phonon peak is well reproduced showing that the long-ranged interactions [38] are effectively captured with the GSP89 model, Fig. 2(a). The energy of the optic peak is strongly overestimated, Fig. 2(a), which leads to a low acoustic-optic phonon scattering resulting in a high κ_l, Fig. 2(c). Also α, which is related to κ_l through the Grüneisen parameters [10,39], shows deviations from DFT results, Fig. 2(b). However, this simple model captures the low temperature negative α for Si in good agreement with DFT and experiment.

The short-ranged KBS94 [35] and GPD15 [37] models used the same functional form as GSP89, Eqs. (14) and (15), for their parametrization [33]. The KBS94 model focused on describing the elastic constants, defect formation energies for vacancies and interstitials in Si crystal, along with the binding energies of different structures. Similarly the more recent GPD15 model was fitted to reproduce the binding energy curves for different structures of Si [37]. The KBS94 and GPD15 models, similar to GSP89, capture the DOS peaks for all three Si structures, but with over- or underestimated bandwidths, Fig. 1. However, unlike GSP89, a poor description of the thermal properties for diamond Si is seen for both KBS94 and GPD15, Fig. 2. The pDOS acoustic peaks and the bandwidths from these models exhibit large deviations from DFT, Fig. 2(a). Furthermore, these models fail to capture low temperature negative α, Fig. 2(b), for Si and predict very high κ_l, in the same order as the Tersoff empirical potential [40], Fig. 2(c).

Interestingly, both WCH89 and GSP89 can be said to give a fair agreement for the thermal properties, whereas the KBS94 and GPD15 give a poor description, Fig. 2. This indicates that

fitting mainly the energy-volume curve of diamond Si can give a good reproduction of both the harmonic and anharmonic contributions to the interatomic potential and the increased fitting data set leads to a better average reproduction of the fitted properties, but a lack of transferability to unfitted properties.

A different approach was taken in LER97 which used cubic splines with seven evenly spaced spline knots as fitting parameters for their pairwise functions [36]. The model is long ranged, with a cutoff around the fourth neighbor shell of diamond Si, and was fitted to a very large data set [36]. Along with the energetics for different structures, the LER97 model was fitted to the experimental elastic constants, phonon frequencies, and Grüneisen parameters for diamond Si. The LER97 gives the best reproduction of thermal properties for diamond Si, Fig. 2. The pDOS shows an excellent bandwidth reproduction, Fig. 2(a). Moreover, fitting the model to the Grüneisen parameters results in a good reproduction of α and κ_l with this model, as seen in Figs. 2(b) and 2(c). However, the LER97 model captures the pDOS of different structures of Si, Fig. 1, reproducing the band gaps only.

The LER97 model shows how a flexible functional form can be fitted to reproduce a wide range of thermal properties. However, the poor reproduction of the electronic properties shows that the model can be thought of as a scheme to reproduce DFT total energies with a simplified functional form, rather than an actual physical model of the individual contributions to the DFT total energy functional.

B. New OTB model for Si: KM1

Within this section we present our OTB model and its parametrization. Based on the above observations, we formulate a recursive strategy for developing a simple short-ranged model for the κ_l of Si. The minimum requirement of the model should be that it reproduces the properties of ground-state structure before its applicability to any other structures. We therefore fit the DOS and the binding energy curve of diamond Si. Flexibility, beyond the short-range pairwise interactions, is then added after checking the transferability.

The binding energy functional in Eq. (10) is used for the new Si OTB model and the GSP89 functional form, Eqs. (14) and (15), is used for its parametrization. Furthermore, for a smooth convergence of β and ϕ to zero, we have used a simple cosine cut-off function of the form

$$f_{\text{cut}}(R) = \begin{cases} \frac{1}{2}\left(\cos\left\{\pi\left[\frac{R-(R_{\text{cut}}-d_{\text{cut}})}{d_{\text{cut}}}\right]\right\} + 1\right), & R_{\text{cut}} - d_{\text{cut}} \leqslant R < R_{\text{cut}}, \\ 1, & R < R_{\text{cut}} - d_{\text{cut}}, \\ 0, & R \geqslant R_{\text{cut}}. \end{cases} \quad (16)$$

R_{cut}, in Eq. (16), is the cut-off distance for the model and d_{cut} determines the range of the cut-off function. To keep our model short ranged, we have used small cutoff of $R_{\text{cut}} = R_c$ in Eq. (16) for both β and ϕ in our model. We have chosen R_c between the first- and the second-neighbor distances.

We have fitted the equilibrium bonding parameters, β^0 in Eq. (14), to the equilibrium diamond Si band structure below Fermi level. The obtained β_0 are listed in Table I and the

pDOS for diamond Si is presented in Fig. 3(a). Figure 3(a) shows an improvement over the earlier TB models, Fig. 1(a), and demonstrates a good reproduction of the DOS bandwidth and its peaks below the Fermi level as compared to DFT.

The GSP89 functional form gives separate parameters to fit the slope of the pairwise functions independently of the equilibrium values, thereby tuning the slope of an energy-volume curve. The bonding slope parameters (n and n_c),

TABLE I. The parameters for the developed Si OTB models, Eqs. (14), (15), and (17). $R_0 = 2.36$ Å, $R_c = R_{cut} = 3.67$ Å, and $d_{cut} = 0.5$ Å.

	$\beta_{ss\sigma}^0$ (eV)	$\beta_{sp\sigma}^0$ (eV)	$\beta_{pp\sigma}^0$ (eV)	$\beta_{pp\pi}^0$ (eV)	$\epsilon_s - \epsilon_p$ (eV)	n	n_c
	-1.67	1.91	1.93	-0.81	-5.60	2.04	11.65
	ϕ^0 (eV)	m	a (meV)	b	R_{peak} (Å)	n_{emb}	R_{cut}^{emb} (Å)	d_{cut}^{emb} (Å)
KM1	1.206	5.680						
KM2	1.250	5.519	0.1504	1.91	3.7	0.57	5.5	1.3

in the KM1 model, are fitted together with the repulsive parameters [ϕ_0 and m in Eq. (15)] to the diamond Si binding energy curve (19 energies at $\pm 27\%$ volume range) and elastic constants (seven energies for each elastic constants: C_{11}, C_{12}, and C_{44} within $\pm 6\%$ volume range maximally). We carried out various fitting tests, including weighting the energies for elastic constants by a factor of 10, fitting equilibrium bonding parameters too, and trying different optimizers, however, we got similar parameters in all the cases. We also tried fitting the model excluding the elastic constants from our fitting data set, however, we found no significant change in our model parameters and the model results. Our model parameters are labeled KM1 in Table I.

The agreement of the KM1 model for the fitted binding energies and the elastic constants of diamond Si with the DFT calculations is demonstrated in Table II. The calculated bulk modulus B_0 shows an excellent comparison to DFT with only 2% deviation. On the other hand, the elastic constants C_{11}, C_{12}, C_{44} with the KM1 model deviate maximally by 32% from DFT results, Table II. However, considering the simplicity and short-ranged behavior of the KM1 model this comparison is reasonable.

The transferability of the KM1 model is tested by applying it to calculate the unfitted thermal properties for diamond Si and energetics for different structures of Si. We have followed Sec. II A to calculate the diamond Si phonon dispersion and α in harmonic and quasiharmonic approximations, respectively, and κ_l by determining anharmonic phonon scattering rates. The phonon dispersion for diamond Si with the KM1 model, Fig. 4(a), is in very good agreement with the DFT results

and performs better than the earlier long- and short-ranged models [33–37], Fig. 2. The acoustic phonons and the phonon bandwidth for diamond Si are well reproduced with the KM1 model which influence further harmonic and anharmonic thermal properties (discussed in Sec. III A).

The α with the KM1 model, which is very sensitive thermal property, is also reproduced in close comparison with DFT, Fig. 4(b). As the KM1 model parameters are fitted to the DFT (PBE) data set, which overestimates the α compared to experiments due to the prediction of softer equilibrium lattice, the α with the KM1 model is also higher than experiments. However, the KM1 model calculated α compares well to the DFT (PBE) results showing that the model captures the trends of the potential to which it is fitted. Furthermore, a good reproduction of negative α shows the success of our short-ranged model for capturing such detailed anharmonic effects.

Finally, Fig. 4(c) shows the calculated κ_l for diamond Si. It can be seen that the KM1 model outperforms the earlier TB models (GSP89 [33], WCH89 [34], KBS94 [35], GPD15 [37]), Fig. 2(c), for prediction of κ_l. Furthermore, the κ_l reproduction with the long-ranged LER97 model [36], fitted explicitly to the Si phonons and Grüneisen parameters, is comparable to the KM1 model, which is simpler and has smaller fitting data set than the LER97 model.

Such an accurate reproduction of the thermal properties confirms that fitting a simple short-ranged OTB model to just the energy-volume cure of diamond Si is able to capture harmonic and anharmonic contributions to the interatomic force constants.

The transferability of the KM1 model to other Si structures, such as clathrate-I and β-tin, is tested by calculating the DOS and the binding energies E_{b_0}, Fig. 3 and Table II, respectively. The DOS for β-tin with the KM1 model, Fig. 3(c), shows an overestimated bandwidth similar to the earlier GSP89 and KBS94 models, however, for the clathrate-I structure, we get an excellent DOS comparison with DFT, Fig. 3(b). Table II shows a fair agreement of E_{b_0} for both β-tin and clathrate-I with KM1 model to DFT. Furthermore, we have also calculated the equilibrium volume V_0 and bulk modulus B_0 for both these structures, Table II, where a good agreement of the KM1 model with DFT is seen. However, KM1 model also predicts more stable clathrate-I Si than the diamond Si with a very small binding energy difference $\Delta E_{b_0} = 17$ meV, Table II, which needs to be rectified.
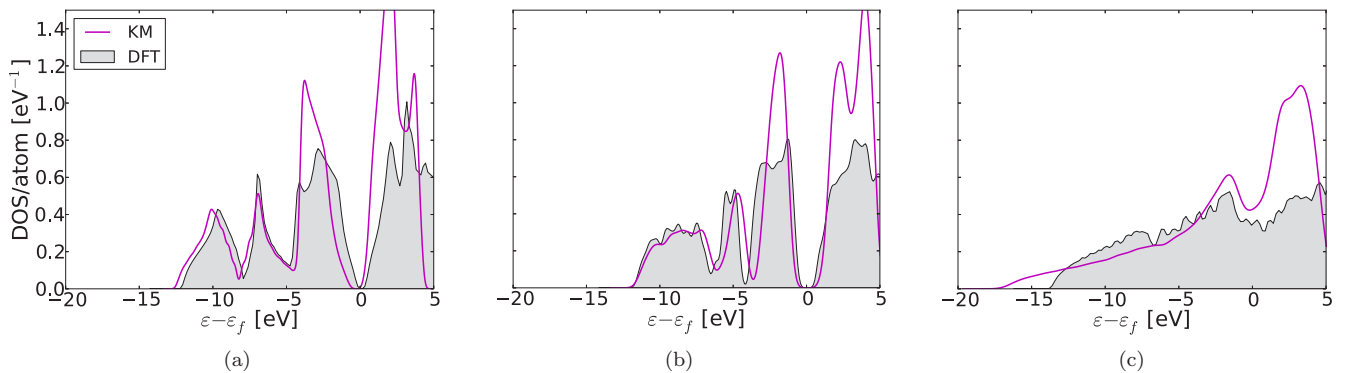

FIG. 3. DOS for Si in (a) diamond, (b) clathrate-I, and (c) β-tin structures at respective DFT optimized volumes calculated using our OTB model (Table I) and compared to DFT.

TABLE II. The equilibrium volume (V_0), binding energy (E_{b_0}), and bulk modulus (B_0) for diamond, clathrate-*I*, and β-tin Si and the elastic constants (C_{11}, C_{12}, C_{44}) for diamond Si with our two models: KM1 and KM2 (Table I), compared to DFT and earlier OTB models.

	Diamond						Clathrate-*I*			β-tin		
	V_0/atom (Å^3)	E_{b_0}/atom (eV)	B_0 (GPa)	C_{11} (GPa)	C_{12} (GPa)	C_{44} (GPa)	V_0/atom (Å^3)	E_{b_0}/atom (eV)	B_0 (GPa)	V_0/atom (Å^3)	E_{b_0}/atom (eV)	B_0 (GPa)
DFT (PBE)	20.44	−5.424	88.65	161	64	77	23.27	−5.361	77.91	15.32	−5.130	108.42
KM1	20.42	−5.423	86.87	122	70	52	23.01	−5.440	78.65	16.07	−5.270	232.89
KM2	20.40	−5.422	84.97	119	69	52	23.07	−5.407	73.96	16.31	−5.169	204.87
DFT (LDA)	19.71	−5.959	96.41	162	65	77	22.46	−5.873	84.13	14.83	−5.749	116.57
GSP89	20.18	−5.465	102.65	147	82	67	22.56	−5.472	94.88	16.55	−4.989	234.20
WCH89	20.19	6.322	92.51	141	69	62	22.59	3.075	84.82	15.36	8.235	125.31
KBS94	20.19	−5.296	85.19	147	55	86	22.96	−5.351	81.38	15.42	−5.083	143.41
LER97	19.99	−4.620	97.64	166	63	76	22.66	−4.561	105.83	16.10	−4.251	149.52
GPD15	19.73	−5.350	96.72	186	53	109	22.15	−5.315	94.23	17.21	−4.894	179.28

C. Including an embedding potential: KM2

To address the crucial problem of our model to predict $E_b^{\text{diamond}} < E_b^{\text{clathrate-}I}$, we have first analyzed the bonding in these structures. Both the clathrate-*I* and diamond structures have four Si nearest neighbors. The number of atoms in the second-neighboring shell for clathrate-*I* (11) is less than for diamond (12) which demonstrates that clathrate-*I* Si is a more open structure than diamond Si.

The difference in atomic coordination between the diamond and clathrate-*I* structures being in the second-neighbor shell, the disagreement between our model and DFT indicates that our short-ranged OTB, with a cutoff between first and second neighbors, does not correctly capture these long-ranged interactions. To analyze this further we have obtained β from a systematic DFT downfolding procedure [41,42] and compared them to our fitted β, Fig. 5. Figure 5 shows that there is a residual bonding contribution between the DFT derived $\beta_{ss\sigma}$ (markers) for diamond Si and the present short-ranged KM1 $\beta_{ss\sigma}$.

We have accounted for this residual contribution by including an embedding potential E_{emb} in Eq. (10) for our model as

$$E_{\text{emb}} = -\sum_I \left[\sum_{J \neq I} \phi_{\text{emb}}(R_{IJ}) \right]^{1/2}, \quad (17)$$

with a square-root dependence on the coordination number [41]. This residual bonding contribution shows skewed Gaussian behavior with a shifted peak around the cutoff of our model, Fig. 5. Thus the ϕ_{emb} in Eq. (17) is given by the functional form

$$\phi_{\text{emb}}(R) = a\{\exp[-b(R - R_{\text{peak}})^2] + R^{n_{\text{emb}}}\}^2, \quad (18)$$

where $R^{n_{\text{emb}}}$ helps to skew the Gaussian function with shifted peak at R_{peak}. The final exponent of 2 is used for smoothening the curve. Moreover, the cosine cut-off function, Eq. (16), is used to converge the ϕ_{emb} to zero.

The parameters of the embedding function are fitted together with the repulsive parameters ϕ_0 and m, Eq. (15), to the binding energy curves for the diamond Si (19 energies at $\pm 27\%$ volume range) and the clathrate-*I*, β-tin Si (11 energies for each structure at $\pm 15\%$ volume range). The rest of the model parameters are fixed to the values in Table I. For the embedding part, we have chosen R_{peak} value near to R_{cut} in Table I. Furthermore, a large and smooth cutoff, with $R_{\text{cut}}^{\text{emb}}$ between the fourth- and fifth-neighbor distance in diamond Si, is used for embedding potential in our model. The final model (KM2) parameters are listed in Table I which shows that the refitted ϕ_0 and m did not change drastically as compared to those of the KM1. The ϕ_{emb} of the KM2 model is seen in
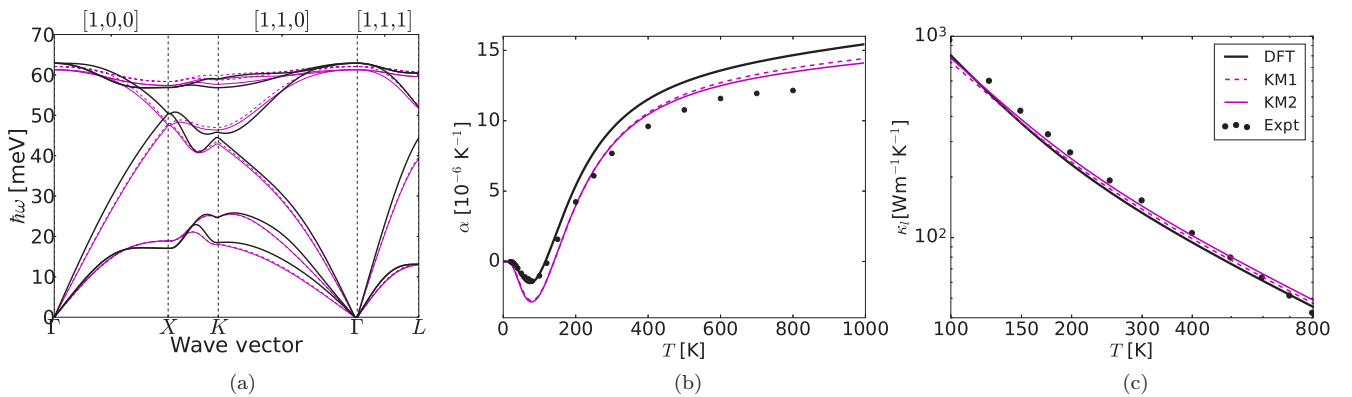

FIG. 4. (a) Phonon dispersion, (b) thermal expansion (α), and (c) lattice thermal conductivity (κ_l) of diamond Si with our two models: KM1 and KM2 (Table I). The overestimation of α as compared to the experiments is because KM1 and KM2 models are fitted to the DFT (PBE) data which has the tendency to predict softer lattice.
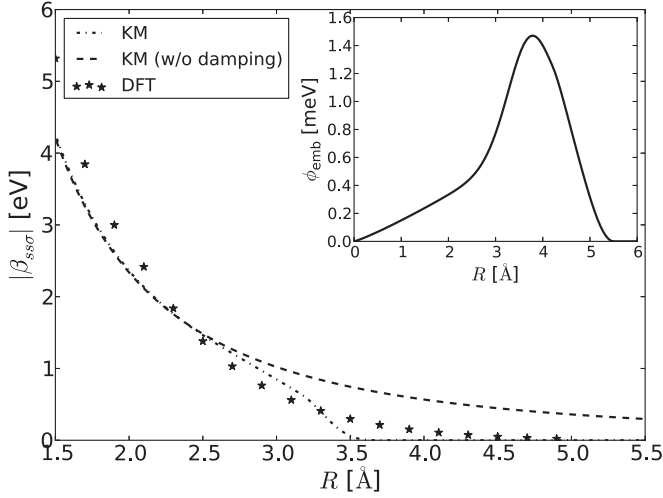
FIG. 5. $\beta_{ss\sigma}$ for diamond Si as a function R with our model, Table I, and obtained from DFT. The residual bonding contribution, not captured with our model, can be seen in the figure which is accounted for by introducing the embedding potential ϕ_{emb} in our model (KM2). The ϕ_{emb} of our model is shown in the inset.

the inset in Fig. 5, which correctly captures the trend of the residual bonding function.

The KM2 model, Table I, is tested for the relative stabilities of the different structures of Si, Fig. 6 and Table II. The binding energy-volume curves for different structures of Si compare well with DFT. A maximum $\Delta E_{b_0}^{\beta\text{-tin}}$ of 39 meV/atom, within the three low-energy Si structures, namely the diamond, clathrate-I, and β-tin, is obtained with the KM2 model, Table II. This shows an improvement over the KM1 model, which has a maximum $\Delta E_{b_0}^{\beta\text{-tin}}$ of 140 meV/atom, Table II. Furthermore, the KM2 model also captures the correct trend of $E_b^{\text{diamond}} < E_b^{\text{clathrate}-I}$, as seen in Table II and Fig. 6.
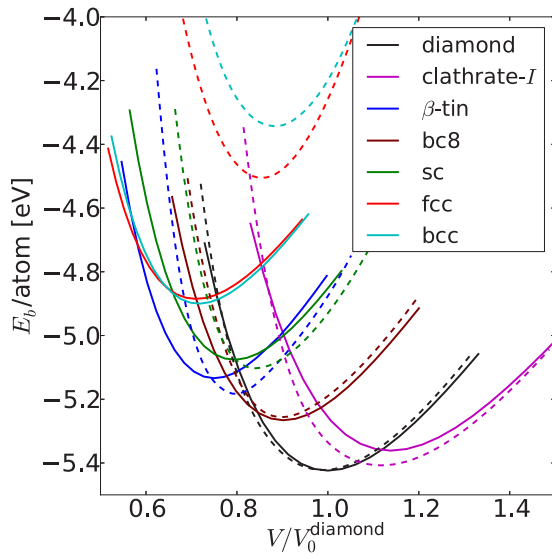

FIG. 6. Binding energy-volume curves for different structures of Si normalized by the diamond Si equilibrium volume calculated with KM2 model (Table I, dashed lines in figure) and compared to DFT results (full lines).
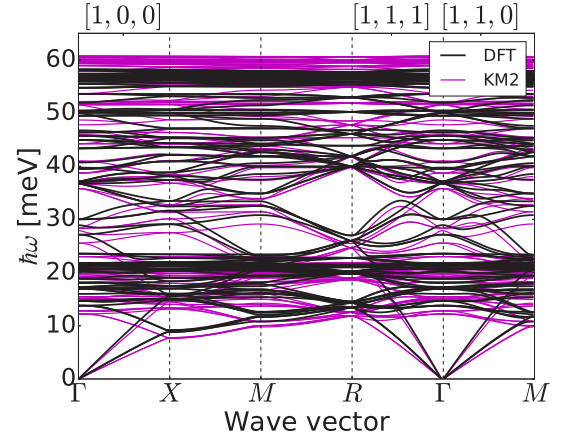

FIG. 7. Phonon dispersion curve of the Si clathrate-I with our KM2 model (Table I).

We have also calculated the equilibrium V_0 and B_0 for diamond, clathrate-I, and β-tin Si and C_{11}, C_{12}, C_{44} for diamond Si with the KM2 model, Table II, and the results are very close to those of the KM1 model. Thus the inclusion of ϕ_{emb} in the KM2 model, Table I, helped us to get correct structural stability trends for different Si structures without affecting the calculations of their further properties, Table II.

The model transferability to reproduce the thermal properties of diamond Si is tested in Fig. 4. The calculated phonon dispersion α and κ_l for diamond Si with the KM2 model are presented in Fig. 4. Similar to the KM1, the phonons α and κ_l for diamond Si are in very good comparison to DFT.

As a final transferability test of the KM2 model, the phonon dispersion for the clathrate-I Si is calculated and compared to DFT results, Fig. 7. The phonon dispersion for clathrate-I Si has similar bandwidth as diamond Si but with more branches and flatter acoustic bands. Despite an overestimation of the phonon bandwidth, the phonon dispersion with the KM2 model shows a good agreement with DFT. The overestimation is due to the smaller equilibrium volume $V_0^{\text{clathrate-}I}$ predicted with our model as compared to DFT, Table II. The parameters and the calculated lattice thermal conductivity using the model

TABLE III. Calculated averaged Grüneisen parameter, reduced Debye temperature, and effective parameters $(\omega^2 \tau_{\text{M}})$ and $\overline{(v/\omega)^2}$, Eq. (5), for the clathrate-I structure. The thermal conductivities κ_l^M at 300 K calculated using the model scattering rates, Eq. (4), are also reported.

Model	$\overline{\gamma}^2$	$\tilde{\theta}_D$ (K)	$(\omega^2 \tau_{\text{M}})$ (10^{15} s^{-1})	$\overline{(v/\omega)^2}$ (10^{-15} J m^{-1} K^{-1})	κ_l^M (W m^{-1} K^{-1})
PBE	0.92	177	5.66	2.59	14.65
KM2	1.08	183	4.39	2.78	12.20
LDA	1.08	181	4.86	2.58	12.54
GSP89	0.64	218	12.36	2.76	34.17
WCH89	0.71	202	9.54	2.82	26.90
KBS94	0.26	253	40.63	2.75	111.52
LER97	0.93	186	6.34	2.71	17.17
GPD15	0.48	236	25.12	2.81	70.65

scattering rate, Eq. (4), are listed in Table III. A very good agreement is observed between the KM2 model and DFT calculated κ_l^{M}. The agreement is partly fortuitous, as the model slightly underestimates the average phonon lifetime $\overline{(\omega^2 \tau_{\mathrm{M}})}$ and overestimates the average phonon velocity $\overline{(v/\omega)^2}$. Our model again represents a significant improvement over the earlier models. Only the LER97 model exhibits a similar good agreement, however with the present model having the advantage of shorter ranged interactions and a simpler construction.

IV. CONCLUSIONS

In this work we have developed a simple and short-ranged OTB model for correctly calculating the thermal properties for different structures of Si. The model is based on the "rescaling method" proposed by GSP89 [33] to parametrize the bonding and repulsive potentials. We have discussed the fitting strategy

and shown how two old short-ranged models correctly reproduce the thermal properties of diamond Si, whereas two newer give results comparable to the Tersoff empirical potentials. Furthermore, we have included an embedding potential, which is found to be important for correctly capturing the structural stability trends of Si. The model is shown to reliably reproduce the energetics of different structures of Si. Furthermore, the transferability of our model is demonstrated by calculating the thermal conductivity and other thermal properties for diamond and clathrate-*I* Si. We have also discussed the improvement of our model over earlier OTB models and empirical interatomic potentials. The model can be used for the MD studies for the thermal properties of different Si nanostructures.

ACKNOWLEDGMENTS

[1] A. I. Boukai, Y. Bunimovich, J. Tahir-Kheli, J. Yu, W. A. Goddard, III, and J. R. Heath, Nature (London) **451**, 168 (2008).

[2] J.-H. Lee, G. A. Galli, and J. C. Grossman, Nano Lett. **8**, 3750 (2008).

[3] M. Strasser, R. Aigner, M. Franosch, and G. Wachutka, Sensors Actuators A **97-98**, 535 (2002).

[4] F. A. Zwanenburg, A. S. Dzurak, A. Morello, M. Y. Simmons, L. C. L. Hollenberg, G. Klimeck, S. Rogge, S. N. Coppersmith, and M. A. Eriksson, Rev. Mod. Phys. **85**, 961 (2013).

[5] E. L. Warren, H. A. Atwater, and N. S. Lewis, J. Phys. Chem. C **118**, 747 (2014).

[6] L. Tsakalakos, J. Balch, J. Fronheiser, B. A. Korevaar, O. Sulima, and J. Rand, Appl. Phys. Lett. **91**, 233117 (2007).

[7] P. Dario, M. C. Carrozza, A. Benvenuto, and A. Menciassi, J. Micromech. Microeng. **10**, 235 (2000).

[8] E. Grigoriev, A. Akindinov, M. Breitenmoser, S. Buono, E. Charbon, C. Niclass, I. Desforges, and R. Rocca, Nucl. Instrum. Methods Phys. Res. Sec. A **571**, 130 (2007).

[9] D. G. Cahill, P. V. Braun, G. Chen, D. R. Clarke, S. Fan, K. E. Goodson, P. Keblinski, W. P. King, G. D. Mahan, A. Majumdar *et al.*, Appl. Phys. Rev. **1**, 011305 (2014).

[10] D. A. Broido, A. Ward, and N. Mingo, Phys. Rev. B **72**, 014308 (2005).

[11] T. Wang, G. K. H. Madsen, and A. Hartmaier, Model. Simul. Mater. Sci. Eng. **22**, 035011 (2014).

[12] A. Skye and P. K. Schelling, J. Appl. Phys. **103**, 113524 (2008).

[13] D. A. Broido, M. Malorny, G. Birner, N. Mingo, and D. A. Stewart, Appl. Phys. Lett. **91**, 231922 (2007).

[14] K. Esfarjani, G. Chen, and H. T. Stokes, Phys. Rev. B **84**, 085204 (2011).

[15] A. Ward, D. A. Broido, D. A. Stewart, and G. Deinzer, Phys. Rev. B **80**, 125203 (2009).

[16] L. Lindsay, D. A. Broido, and T. L. Reinecke, Phys. Rev. B **87**, 165201 (2013).

[17] J. Garg, N. Bonini, B. Kozinsky, and N. Marzari, Phys. Rev. Lett. **106**, 045901 (2011).

[18] A. Katre, A. Togo, I. Tanaka, and G. K. H. Madsen, J. Appl. Phys. **117**, 045102 (2015).

[19] P. Erhart, P. Hyldgaard, and D. O. Lindroth, Chem. Mater. **27**, 5511 (2015).

[20] D. R. Bowler and T. Miyazaki, Rep. Prog. Phys. **75**, 036503 (2012).

[21] P. E. Blöchl, Phys. Rev. B **50**, 17953 (1994).

[22] G. Kresse and D. Joubert, Phys. Rev. B **59**, 1758 (1999).

[23] J. P. Perdew and Y. Wang, Phys. Rev. B **45**, 13244 (1992).

[24] J. P. Perdew, K. Burke, and M. Ernzerhof, Phys. Rev. Lett. **77**, 3865 (1996).

[25] A. Togo and I. Tanaka, Scr. Mater. **108**, 1 (2015).

[26] L. Chaput, A. Togo, I. Tanaka, and G. Hug, Phys. Rev. B **84**, 094302 (2011).

[27] A. Togo, L. Chaput, and I. Tanaka, Phys. Rev. B **91**, 094306 (2015).

[28] L. Bjerg, B. B. Iversen, and G. K. H. Madsen, Phys. Rev. B **89**, 024304 (2014).

[29] G. K. H. Madsen, A. Katre, and C. Bera, Phys. Status Solidi (a) **213**, 802 (2016).

[30] J. C. Slater and G. F. Koster, Phys. Rev. **94**, 1498 (1954).

[31] H. Ibach, Phys. Status Solidi (b) **31**, 625 (1969).

[32] C. J. Glassbrenner and G. A. Slack, Phys. Rev. **134**, A1058 (1964).

[33] L. Goodwin, A. J. Skinner, and D. G. Pettifor, Euro. Phys. Lett. **9**, 701 (1989).

[34] C. Z. Wang, C. T. Chan, and K. M. Ho, Phys. Rev. B **39**, 8586 (1989).

[35] I. Kwon, R. Biswas, C. Z. Wang, K. M. Ho, and C. M. Soukoulis, Phys. Rev. B **49**, 7242 (1994).

[36] T. J. Lenosky, J. D. Kress, I. Kwon, A. F. Voter, B. Edwards, D. F. Richards, S. Yang, and J. B. Adams, Phys. Rev. B **55**, 1528 (1997).

[37] J. Gehrmann, D. G. Pettifor, A. N. Kolmogorov, M. Reese, M. Mrovec, C. Elsässer, and R. Drautz, Phys. Rev. B **91**, 054109 (2015).

[38] A. Katre, R. Drautz, and G. K. H. Madsen, J. Phys. Condens. Matter **25**, 365403 (2013).

[39] N. W. Ashcroft and N. D. Mermin, *Solid State Physics* (Holt, Rinehart and Winston, New York, 1976).

[40] J. Tersoff, Phys. Rev. B **37**, 6991 (1988).

[41] G. K. H. Madsen, E. J. McEniry, and R. Drautz, Phys. Rev. B **83**, 184119 (2011).

[42] A. Urban, M. Reese, M. Mrovec, C. Elsässer, and B. Meyer, Phys. Rev. B **84**, 155119 (2011).